Journal Name

ARTICLE

Manganese Dioxide Nanosheets Functionalizing Sulfur@PEDOT Core-Shell Nanospheres for Advanced Lithium-Sulfur Batteries

Received 00th January 20xx,
Accepted 00th January 20xx

DOI: 10.1039/x0xx00000x

www.rsc.org/

Min Yan,[a] Yang Zhang,[a] Yu Li,[a *] Yongqi Huo,[a] Yong Yu,[a] Chao Wang,[a] Jun Jin,[a] Lihua Chen,[a] Tawfique Hasan,[b] Binjie Wang[c] and Bao-Lian Su[a,d,e *]

Lithium-sulfur (Li-S) batteries are receiving significant attention as an alternative power system for advanced electronic devices because of their high theoretical capacity and energy density. In this work, we have designed manganese dioxide (MnO_2) nanosheets functionalized sulfur@poly(3,4-ethylenedioxythiophene) core-shell nanospheres (S@PEDOT/MnO_2) for high performance lithium-sulfur (Li-S) batteries. The PEDOT layer is used to address the low electrical conductivity of sulfur and acts as protective layer to prevent dissolution of polysulfides. The MnO_2 nanosheets functionalizing on PEDOT further provide high active contact area to enhance the wettability of the electrode materials by electrolyte and further interlink the polymer chains to improve the conductivity and stability of the composite. As a result, S@PEDOT/MnO_2 exhibits an improved capacity of 827 mAh g^{-1} after 200 cycles at 0.2 C (1C=1673 mA g^{-1}), a further ~50% enhancement comparing to S@PEDOT (551 mAh g^{-1}) without MnO_2 functionalization. In particular, the discharge capacity of S@PEDOT/MnO_2 is 545 mAh g^{-1} after 200 cycles at 0.5 C. Our demonstration here indicates that the functionalization of inorganic nanostructures on conducting polymer coated sulfur nanoparticles is an effective strategy to improve the electrochemical cycling performance and stability of sulfur cathodes for Li-S batteries.

1. Introduction

The widespread usage of portable electronic devices and rapid growth of electric vehicles require the development of next-generation batteries with higher capacity and energy density. To achieve a quantum leap in the specific energy density of current generation batteries, new electrode materials with high storage capacity are required.[1-2] Indeed, over the past few years, extensive research has been conducted on the development of such high capacity electrode materials.[3-5] Amongst the next generation battery systems with high energy storage, the lithium-sulfur (Li-S) batteries are considered very attractive. Elemental sulfur has a high theoretical capacity of 1673 mAh g^{-1} and an energy density of 2600 Wh kg^{-1}. These are much higher than the conventional cathode materials (capacity of ~250 mAh g^{-1} and energy density of ~400 Wh kg^{-1}) in lithium-ion batteries.[6-10] In addition, sulfur exhibits many other favorable characteristics, including abundance, low toxicity, environmental friendliness and low cost.[11-13]

Despite these advantages, practical scale-up applications of Li-S batteries are hindered by low conductivity (5×10^{-30} S cm^{-1} at 25 °C) and large volumetric expansion of sulfur upon lithiation (~80%).[14] In particular, the discharge reaction of sulfur involves stepwise reduction processes and produces various forms of soluble intermediate lithium polysulfides. These can dissolve in the liquid electrolyte and cause a rapid irreversible loss of active materials upon repeated cycling. In addition, the high solubility of the intermediate lithium polysulfides can move to lithium anode and be reduced to short-chain polysulfides, which move back to the cathode and are reoxidized into long-chain polysulfides, called shuttle effect. This further reduces the coulombic efficiency and the cycle life of Li-S batteries.[15]

To address these aforementioned challenges of Li-S batteries, great strides have been made in the past several years. For example, Nazar and co-workers have pioneered the concept of using ordered mesoporous carbon to constrain sulfur within its channels, followed by modification of polyethylene glycol, providing a chemical gradient to retard diffusion of soluble polysulfides out of the electrode. This approach addresses the conductivity issue and improve trapping of polysulfides, resulting in a high reversible capacity.[16] Various other carbon nanostructures have then been used to produce sulfur-carbon composites, such as carbon nanofiber,[17] carbon nanotube,[18] carbon hollow sphere,[19] micro/mesoporous carbon,[20] and graphene.[21] However, sulfur still diffuses out from open-pore structure of carbon during the charge-discharge process. This is due to weak intermolecular interactions between the nonpolar

[a] State Key Laboratory of Advanced Technology for Materials Synthesis and Processing, Wuhan University of Technology, 122 Luoshi Road, 430070, Wuhan, Hubei, China; Email: yu.li@whut.edu.cn; baoliansu@whut.edu.cn.
[b] Cambridge Graphene Centre, University of Cambridge, 9 JJ Thomson Avenue, Cambridge CB3 0FA, United Kingdom.
[c] FEI Company, Shanghai Nanoport, 399 Shengxia Road, 201210 Shanghai, China
[d] Laboratory of Inorganic Materials Chemistry (CMI), University of Namur, 61 rue de Bruxelles, B-5000 Namur, Belgium; E-mail: bao-lian.su@unamur.be
[e] Department of Chemistry and Clare Hall, University of Cambridge, Cambridge, CB2 1EW, United Kingdom; E-mail: bls26@cam.ac.uk
† Electronic Supplementary Information (ESI) available: the R_{ct} values, the increasement of the R_{ct} values and the digital photographs of the S-NPs, S@PEDOT and S@PEDOT/MnO2 electrodes before and after 200 cycles. See DOI: 10.1039/x0xx00000x

carbon and polar Li_xS clusters ($0<x\leq2$) as well as the physical encapsulation of sulfur insufficiently alleviating the dissolution of polysulfides in a long term.[22] Moreover, the fabrication of the sulfur-carbon composites usually requires elaborate procedures, involving high-temperature process or corrosive acid.[19,20] These defects significantly limit the manufacturability of the sulfur-carbon cathode materials.

Alterlatively, conducting polymers such as polyaniline (PANI),[23-25] poly(3, 4-ethylenedioxythiophene) (PEDOT),[26,27] polydopamine (PDA),[28,29] and polypyrrole (PPY),[30,31] have aroused much attention to improve the performance of Li-S batteries due to their flexibility, good electrochemical stability, simple preparation and favorable morphologies.[32-34] For example, Zhao and co-workers have prepared core-shell sulfur-polythiophene composite, in which polythiophene acts as a conducting additive and a porous adsorbing agent, enhancing the electrochemical performance of sulfur electrode (830.2 mAh g^{-1} at 100 mA g^{-1} after 80 cycles).[35] Chen and co-workers have prepared sulfur nanoparticles with an outer conducting PEDOT layer. This provides abundant electron transport active sites while acting as a protective layer to prevent dissolution of polysulfides.[36] Although conducting polymer coating on sulfur can effectively improve electron transport and protect the dissolution of polysulfides in electrodes, the electrochemical performance of sulfur-conducting polymer composites is still not good enough. We suppose that the limited improvement is due to the low contact area and poor wettability of the conducting polymer network electrode with the electrolyte, and again the dissolution of polysulfides. We then propose that functionalizing a thin layer on to the conducting polymer chains could strengthen the interlink between them, as well as increase the contact area and wettability of the polymer network with electrolyte. This could enhance the electrochemical performance of Li-S batteries.

Herein, we report MnO_2 nanosheets (MnO_2-NSs) functionalizing sulfur@PEDOT core-shell nanoparticles (S@PEDOT/MnO_2) for Li-S batteries. Flexible PEDOT, due to its high electrical conductivity (550 S/cm) and excellent electrochemical stability, is used to address the low electrical conductivity of sulfur nanoparticles (S-NPs) and prevent polysulfide dissolution. It has also been reported that a nanosheet-based shell could provide a stable, porous framework, effective grain boundaries and a short diffusion pathway for Li^+ and electron transport.[37] Thus, we further functionalize the PEDOT layer with MnO_2-NSs by a facile soaking process. We expect that the MnO_2-NSs functionalization over the conducting polymer network could provide high active contact area and enhance the wettability of the electrode. Such functionalization could further improve the conductivity and stability of sulfur cathode via interlinking the polymer chains and MnO_2-NSs. Importantly, there exist electrochemically interactions between Li^+ and MnO_2, leading to the generation of a more stabilized shelly structure. This shelly structure can function as a robust protective layer to entrap sulfur and lithium polysulfides inside the cathodes, hence efficiently extending the cell cycle lifespan. Moreover, metal oxides such as MnO_2 possess hydrophilic Mn-O groups and surface hydroxyl groups, which may enhance the interaction between the MnO_2 and sulfur, further bind favorably with polysulfides anions. This could permit fixed confinement of sulfur/polysulfides, restrain the reaction kinetic hindrance and minimize shuttle effect. Indeed, using these requirements as design guidelines, our fabricated S@PEDOT/MnO_2 demonstrates very good electrochemical performance, with a stable capacity up to 827 mAh g^{-1} at 0.2 C after 200 cycles. Even at 0.5 C after 200 cycles, a discharge capacity of 545 mAh g^{-1} is achieved.

2. Experiment Section

2.1 S-NPs preparation

All the chemicals are bought from Sigma-Aldrich in ACS reagent. The S-NPs are synthesized by adding concentrated HCl (0.8 ml, 10 M) to an aqueous solution of $Na_2S_2O_3 \cdot 5H_2O$ (100 ml, 0.04 M) containing a low concentration of polyvinylpyrrolidone (Mw ~55,000). After reaction for 2 h, the sulfur NPs (100 ml) are washed by centrifugation and redispersed in water.

2.2 S@PEDOT preparation

120 µL of 3, 4-ethylenedioxythiophene (EDOT), 0.12g camphorsulfonic acid and 0.6g $(NH_4)_2S_2O_8$ are added into the solution of S-NPs. The mixture is stirred at room temperature till the color of the suspension is changed to greyish-green. The precipitates are then isolated from the solution by centrifugation.

2.3 S@PEDOT/MnO_2 preparation

MnO_2-NSs are grown on to S@PEDOT by soaking the as-prepared S@PEDOT in 10 mM $KMnO_4$ solution for 5 min. The products are then washed repeatedly with ethanol and deionized water. The brown powder obtained this way is next dried at 60 °C for 12 h.

2.4 Characterizations

X-ray diffraction (XRD) patterns are obtained using a Bruker diffractometer at 40 kV, 40 mA, with Cu Kα radiation (λ=1.54056 Å). X-ray photoelectron spectroscopy (XPS) analysis is done on a VG Multilab 2000. The thermogravimetric (TG) analysis is recorded by using a thermal analyzer (Setaram, Labsys Evo) in nitrogen atmosphere with temperature ramp of 5 °C min^{-1}. The morphology of all the products is performed on Hitachi S-4800 scanning electron microscopy (SEM) equipped with a field-emission gun at an accelerating voltage of 5 kV. Transmission electron microscopy (TEM), high resolution transmission electron microscopy (HRTEM), high angle annular dark field-scanning transmission electron microscopy (HAADF-STEM) and scanning transmission electron microscopy-energy dispersive spectroscopy (STEM-EDS) are performed on FEI Talos-200X at an accelerating voltage of 200 kV. Contact angle (CA) measurements are performed using an OCA35 automatic contact angle instrument.

2.5 Electrochemical measurement

The working electrodes are prepared by mixing 75 wt% active materials, 15 wt% acetylene black and 10 wt% polyvinylidene fluoride (PVDF) binder in N-methyl pyrrolidinone (NMP). The slurries are homogeneously coated on to aluminum foil current collectors. The electrodes are dried at 60 °C for 12 h under vacuum. Subsequently, the electrodes are cut into disks with a diameter of

12 mm. The CR2025 coin-type cells are fabricated as the working electrodes and lithium metal foils as the counter electrodes. The electrolyte is 1.0 M lithium bis(trifluoromethanesulfonyl)imide (LiTFSI) in 1,3-dioxolane and 1,2-dimethoxyethane (volume ratio, 1:1) with 1 wt% $LiNO_3$ as an additive. The $LiNO_3$ is added to help passivate the surface of the lithium anode and to reduce shuttle effect. The coin cells are assembled in an argon atmosphere glove box. The galvanostatic charge/discharge tests are carried out on a LAND CT2001A battery tester in a potential range of 1.4-2.8 V (versus Li/Li^+). Cyclic voltammetry (CV) (scan rate: 0.1 mV s^{-1}, cut-off voltage: 1.4-2.8 V) is studied using a CHI 660D electrochemical workstation. Electrochemical impedance spectra (EIS) are measured with an electrochemical workstation (Autolab PGSTAT 302N) in the frequency range from 100 kHz to 10 mHz. We note that the specific capacities are based on the mass of sulfur only.

3. Result and discussion

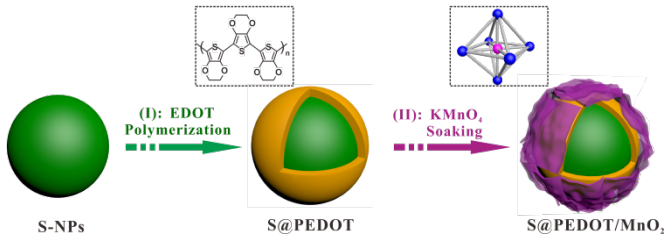

Scheme 1. Schematic illustration for the synthesis of the S@PEDOT/MnO_2 composite.

The fabrication process sequence, starting from S-NPs to S@PEDOT and then to S@PEDOT/MnO_2 is illustrated in Scheme 1. The monodispersed S-NPs are firstly synthesized in aqueous solution of sodium thiosulfate and hydrochloric acid in the presence of PVP at room temperature. As can be seen from the large-area scanning electron microscopy (SEM) in Fig. 1a, the monodispersed S-NPs have almost spherical shape, with ~500 nm diameter. We note that S-NPs have a rough surface, owing to the SO_2 bubble generation during the synthesis (Fig. 1b). Compared to the conducting polymer-coated sulfur composite with >1 μm particle diameter reported previously,[38] our S-NPs, with a smaller diameter (~500 nm) is expected to improve the Li^+ transportation and the electrochemical availability of sulfur.

Next, the PEDOT layer is coated on S-NPs by *in-situ* chemical oxidative polymerization of 3,4-ethylenedioxythiophene (EDOT) monomer. In this process, EDOT, camphorsulfonic acid and $(NH_4)_2S_2O_8$ oxidant are added into the S-NPs suspension under moderate stirring at room temperature. This reaction yields the PEDOT layer on S-NPs outer surface (Scheme 1 and Fig. 1c). After PEDOT coating, the diameter of S@PEDOT do not noticeably increase. However, an obvious uniform thin shell is formed around the outer surface of S-NPs, presenting a visible core-shell structure (Fig. 1d). Definitely, the flexible PEDOT shell will accommodate the volume expansion of sulfur during lithiation, improve the electrical conductivity of the whole composite, and alleviate polysulfides dissolution.

Finally, a simple method is used to anchor amorphous MnO_2 nanosheets onto the S@PEDOT surface via the redox exchange of permanganate ions with the functional group on PEDOT by facile soaking in $KMnO_4$ solution (Scheme 1 and Fig. 1e). The obtained S@PEDOT/MnO_2 keeps the spherical morphology, while a MnO_2 layer is uniformly grown on to the surface of PEDOT. Fig. 1f shows MnO_2 nanosheets anchoring on to the PEDOT layer. We argue that the rough surface of S@PEDOT/MnO_2 provides larger contact area to enhance the wettability of electrode with electrolyte and promote a short diffusion pathway for Li^+ and electron transport. This further improves the electrochemical performance of S@PEDOT/MnO_2. In addition, the double barrier of conductive PEDOT nanolayer and MnO_2-NSs on S-NPs could effectively suppress the loss of active material and reduce the shuttle effect during the charge/discharge processes, as illustrated in Fig. 1g.

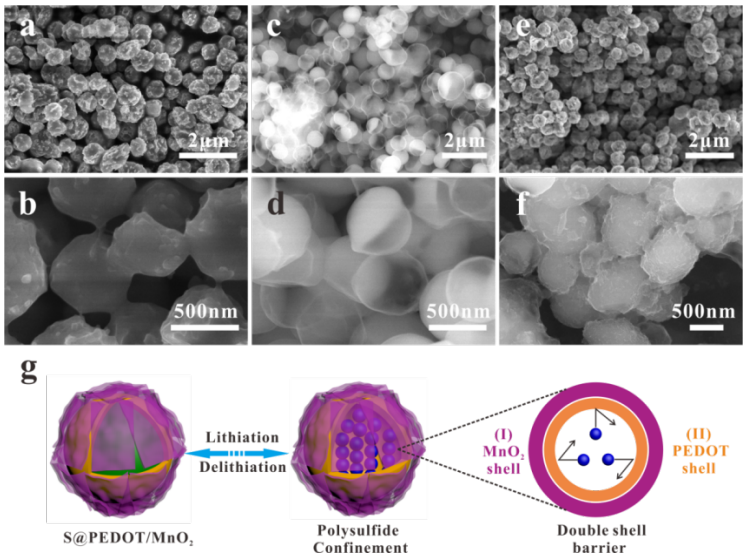

Fig. 1 Typical low and high magnification SEM images of all the products. (a-b) S-NPs, (c-d) S@PEDOT, (e-f) S@PEDOT/MnO_2 and (g) schemed double barrier in S@PEDOT/MnO_2.

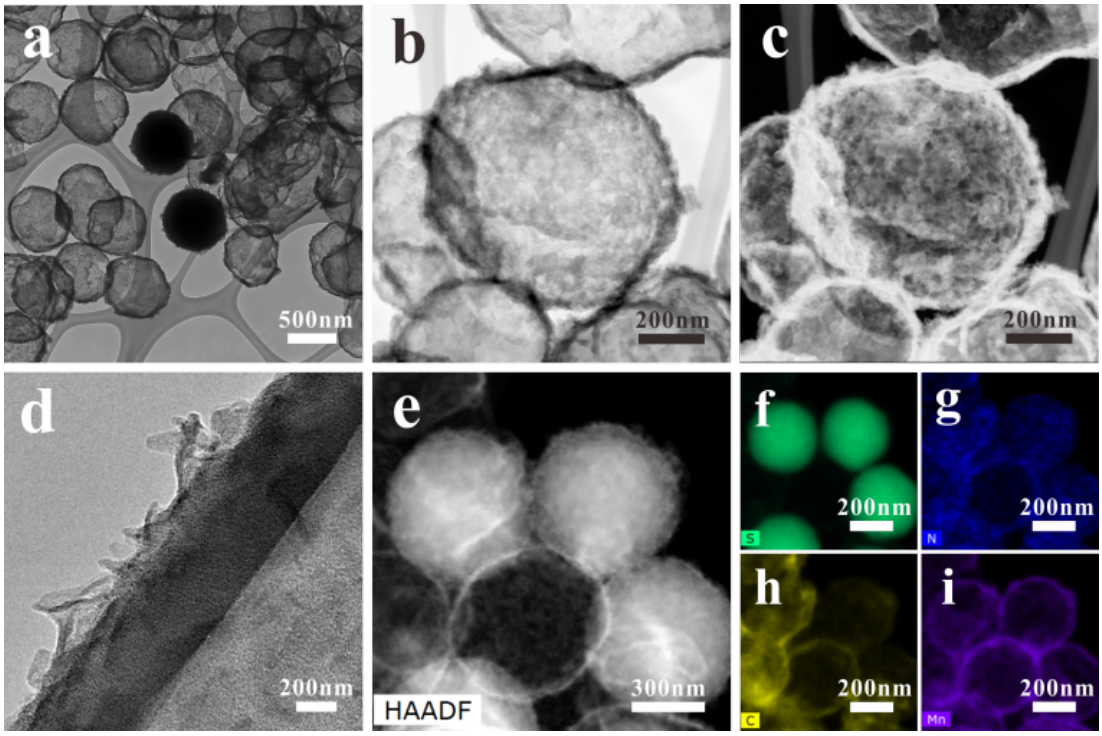

Fig. 2 TEM characterizations of S@PEDOT/MnO_2. (a) bright field (BF) image at low magnification, (b) BF image at high magnification, (c) dark field (DF) image, (d) HRTEM image of the PEDOT layer and MnO_2 nanosheets, (e) HAADF image, and EDS mapping of (f) S, (g) N, (h) C and (i) Mn.

Transmission electron microscopy (TEM) is used to identify the heterostructure of S@PEDOT/MnO_2. As sulfur is easily sublimated under electron beam irradiation, we here use toluene to dissolve most of the sulfur in S@PEDOT/MnO_2 via swelling of PEDOT (This process is very important to avoid the comtamination of sublimiated sulfur to the microscope). Fig. 2a displays a large-area image of S@PEDOT/MnO_2 after toluene treatment. Both the hollow spherical shape and some solid nanospheres with the sulfur inside are observed, indicating the core-shell heterostructure. Fig. 2b and 2c present the bright field (BF) and dark field (DF) image at the same area for several nanoparticles, respectively. These show S@PEDOT/MnO_2 with a rough surface. HRTEM image of the PEDOT/MnO_2 layer outside S-NPs confirms that some MnO_2-NSs finely anchor on to the PEDOT layer (Fig. 2d). We do not observe obvious lattice fringes, confirming the amorphous crystalline states of the PEDOT and MnO_2-NSs. Fig. 2e presents the high angle annular dark field-scanning transmission electron microscopy (HAADF-STEM) image, clearly displaying the core-shell heterostructure. Fig. 2f-i demonstrates the corresponding scanning transmission electron microscopy-energy dispersive spectroscopy (STEM-EDS) mapping profiles of S@PEDOT/MnO_2. These images show that S, N, C and Mn are uniformly distributed in S@PEDOT/MnO_2, confirming that the MnO_2-NSs functionalized PEDOT layer uniformly coats S-NPs. No obvious scattered MnO_2-NSs are observed after strong sonication for 30 min, indicating that MnO_2-NSs are strongly anchored on PEDOT shell.

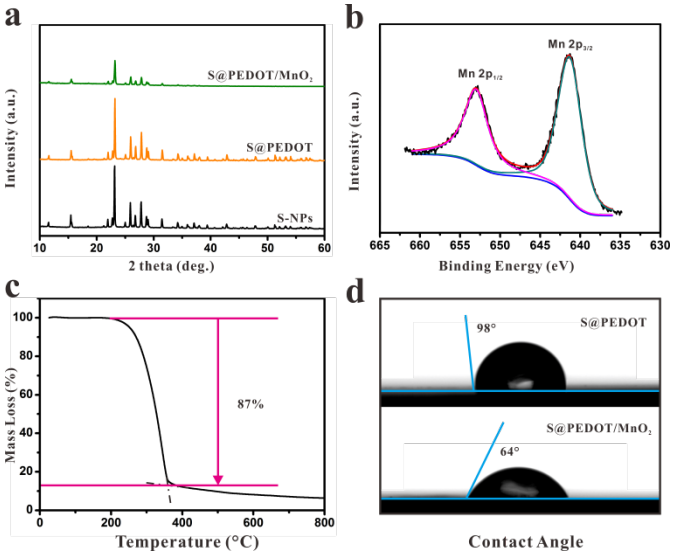

Fig. 3 (a) XRD patterns of S-NPs, S@PEDOT, and S@PEDOT/MnO_2. (b) XPS spectra of S@PEDOT/MnO_2 for Mn 2p. (c) TGA curve of S@PEDOT/MnO_2. (d) Contact angle measurement of S@PEDOT and S@PEDOT/MnO_2.

The X-ray diffraction (XRD) measurements are conducted to determine the phase structure of stepwise products (Fig. 3a). The peaks of S-NPs centering at 23.4 ° and 28.0 ° match well with the (222) and (040) reflections of *Fddd* orthorhombic phase of sulfur (JCPDS No. 08-0247).[39] The sharp and strong diffractions indicate a well-defined crystal structure. No peaks

from other phases are detected, indicating a high purity of S-NPs. Both the characteristic peaks of S@PEDOT and S@PEDOT/MnO_2 are similar to those of S-NPs. This confirms the amorphous phases of PEDOT and MnO_2-NSs, consistent with the TEM observations.

The X-ray photoelectron spectroscopy (XPS) spectrum of S@PEDOT/MnO_2 is presented in Fig. 3b. It shows the peaks of Mn $2p_{3/2}$ and Mn $2p_{1/2}$ locate at 641.8 and 653.5 eV, respectively, corresponding to the spin energy in MnO_2 according to the previous studies.[40,41]

The thermogravimetric (TG) measurement is further used to determine the sulfur content in S@PEDOT/MnO_2. Fig. 3c displays the TG curve of S@PEDOT/MnO_2 obtained in N_2 atmosphere. The weight loss at 170-350 °C corresponds to sulfur sublimation.[16] Therefore, the sulfur content of S@PEDOT/MnO_2 is calculated to be 87 wt%.

Contact angle measurement with water droplets is conducted to investigate the wettability of the electrode material with electrolyte (Fig. 3d). Without MnO_2 functionalization, S@PEDOT demonstrates the contact angle of 98° ± 0.5°, suggesting a relative hydrophilic surface. However, the contact angle of S@PEDOT/MnO_2 decreases to 64° ± 0.5° after MnO_2-NSs modification. This indicates a more hydrophilic surface and the existence of lower surface tension between electrolyte and S@PEDOT/MnO_2 interface, confirming that the S@PEDOT/MnO_2 surface becomes more hydrophilic and could be beneficial for the electrolyte wetting, permeating and preserving.

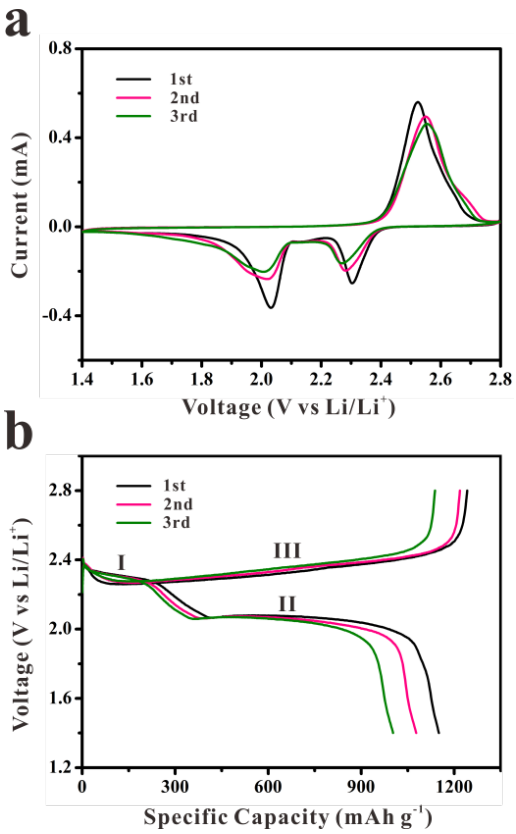

Fig. 4 (a) CV curves of S@PEDOT/MnO_2 at a sweep rate of 0.1 mV/s. (b) Voltage profiles of S@PEDOT/MnO_2 at 0.2 C.

To evaluate the structural benefits of the double modification (metal oxide-polymer) of S@PEDOT/MnO_2 composites for improving the cathodic performance, a series of electrochemical measurements are investigated using 2025-type coin cells with metallic Li foil as the counter electrode. Figure 4a shows the CV curves of the S@PEDOT/MnO_2 electrode at a sweep rate of 0.1 mV/s in the voltage range of 2.8 - 1.4 V for the first three cycles. Two main reduction peaks are observed at ~2.3 and ~2.0 V during the cathodic scan, suggesting a two-step reduction of sulfur. The peak at ~2.3 V corresponds to the reduction of sulfur and electrolyte to form lithium polysulfides (Li_2S_n, 4≤n<8).[42] This can be expressed by the following two equations:

$$Li_2S_x + Li_2S \rightarrow Li_2S_{x-y} + Li_2S_{1+y} \quad (1)$$

$$Li_2S_x + Li_2S_2 \rightarrow Li_2S_{x-y} + Li_2S_{2+y} \quad (2)$$

where x-y and 1+y are larger than 2. The peak at ~2.0 V represents the decomposition of the polysulfides chain in lithium polysulfides to produce insoluble lithium sulfide (Li_2S_2 and/or Li_2S). In the oxidation process, the main peak at ~2.6 V corresponds to the transformation of Li_2S_2 and/or Li_2S into polysulfides. High oxidation potential in CV is attributed to the polarization caused by the phase transition from insoluble Li_2S and/or Li_2S_2 to soluble short-chain polysulfides. In the successive cycles, the oxidation peaks decrease as the cycling increases, the two reduction peaks are relatively stable, indicating good electrochemical stability of S@PEDOT/MnO_2, in which the double barrier of conductive PEDOT nanolayer and MnO_2-NSs on S-NPs effectively suppresses the loss of active material, restrains the reacion kinetic hindrance, and also reduces shuttle effect during the charge/discharge processes.

Fig. 4b depicts the discharge/charge voltage profiles for the first three cycles of the S@PEDOT/MnO_2 electrode at a current density of 0.2 C (1 C=1673 mA g^{-1}). The three voltage plateaus is similar to the redox peaks in the CV tests with two voltage plateaus (I and II) upon discharging and one voltage plateaus (III) upon charging. The initial discharge of the S@PEDOT/MnO_2 electrode shows a high capacity of 1150 mAh g^{-1}. The two discharge voltage plateaus appear at ~2.3 and ~2.0 V, assigned to the two-step reactions mentioned above during the discharge process. In the charge curve, the voltage plateau at ~2.3 V corresponds to the oxidation process, indicating reduced shuttle effect involving the conversion between short-chain polysulfides and long-chain polysulfides.

Fig. 5a shows the cycling performances of the S-NPs, S@PEDOT and S@PEDOT/MnO_2 electrodes at the current density of 0.2 C, respectively. The S-NP electrode exhibits the poorest electrochemical behavior with rapid decay in specific capacity and short cyclic life. The initial discharge capacity is 626 mAh g^{-1}. However, it quickly declines to a low capacitive value (83 mAh g^{-1} after 200 cycles), representing only 13.3% of the initial capacity. This is a typical cyclic behavior of Li-S batteries with liquid electrolyte. As the active sulfur directly contacts the electrolyte, soluble intermediate polysulfides cause a serious shuttle effect in the battery system, resulting in a loss of active sulfur. Moreover, a fraction of the yielded polysulfides molecules migrates out of the cathode and

deposits on lithium anode, which may not be reversibly used again. In addition, undesired side reactions between these highly reactive polysulfides anions and electrolyte solvents can also accelerate the capacity loss.[6, 7]

In comparison, for the S@PEDOT electrode, its cycle life is greatly improved after the PEDOT coating. The initial discharge capacity of the S@PEDOT electrode is 1093 mAh g^{-1} at 0.2 C. The capacity slowly fades to 551 mAh g^{-1}, indicating capacity retention of 50.4% after 200 cycles. Generally, at the beginning of the cycle, some lithium polysulfides could dissolve into the liquid electrolyte resulting in a loss of capacity. Afterward, PEDOT shell could become a stable interface between liquid electrolyte and lithium polysulfides, allowing Li^+ to pass through and charge transfer, and effectively preventing soluble lithium polysulfides from dissolving into electrolyte during cycling. In addition, the highly conducting PEDOT shell in S@PEDOT provides abundant electron transport active sites that enable the quick transfer of electrons.

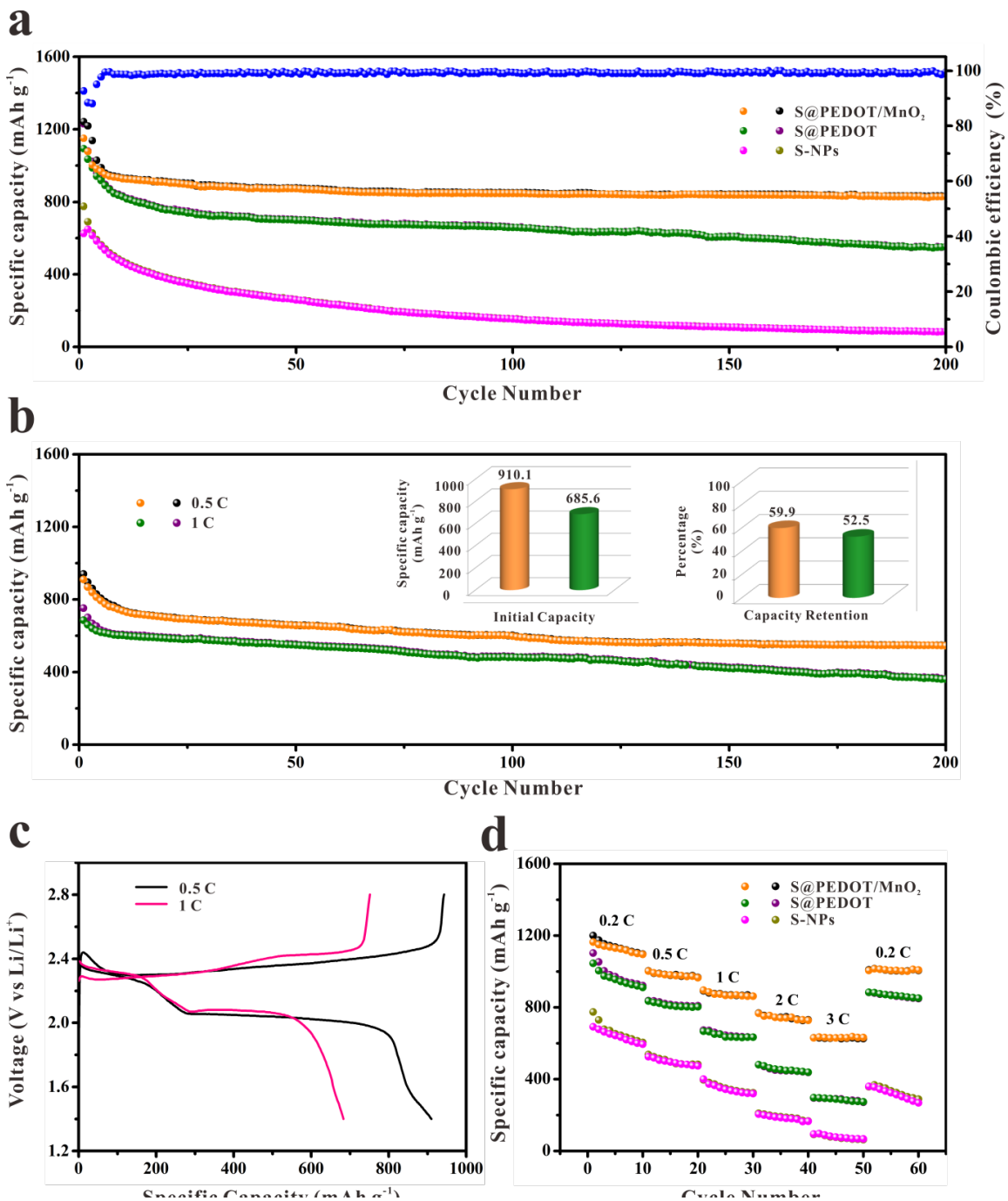

Fig. 5 (a) The cycling performances of the S-NPs, S@PEDOT, and S@PEDOT/MnO_2 electrodes at a current density of 0.2 C. (b) The cycling performance of S@PEDOT/MnO_2 electrode at 0.5 and 1.0 C. The insets are the corresponding initial discharges capacities and capacity retensions. (c) Voltage profiles of S@PEDOT/MnO_2 electrodes cycled at current densities of 0.5 and 1.0 C. (d) The rate performance of the S-NPs, S@PEDOT, and S@PEDOT/MnO_2 electrodes at various current densities from 0.2 to 3.0 C.

In particular, after the incorporation of MnO_2-NSs, the initial discharge capacity of the S@PEDOT/MnO_2 electrode is 1150 mAh g^{-1} and it still remains at 827 mAh g^{-1} after 200 cycles, corresponding to a capacity retention of 71.9% and a small decay of 0.14% per cycle. This demonstrates a ~50.1% capacity enhancement compared to S@PEDOT (551 mAh g^{-1}). Also impressively, the coulombic efficiency still remains over 98% after such long-term cycling, indicating its intrinsic reversibility even at long-term cycling. This is very important for its further commercial application. We argue that the improved performance of S@PEDOT/MnO_2 results from the MnO_2-NSs modification. The MnO_2-NSs grown on S@PEDOT surface can provide high active surface area to improve the wettability of electrode material with the electrolyte to enhance the reaction kinetics. On the other hand, the MnO_2-NSs are beneficial for Li^+ easily access to the cathode surface by interspace diffusions and adsorption: $(MnO_2)_{surface} + Li^+ + e^- \leftrightarrow (MnOOLi)_{surface}$.[9,43] Moreover, MnO_2-NSs can strengthen the interlink of the PEDOT network and act as a further protective layer to entrap the polysulfides inside the cathodes, hence efficiently extending the cycle lifespan. Therefore, the performance of our S@PEDOT/MnO_2 electrode is higher than many previously reported sulfur composites with conducting polymers and even carbon materials.[35,36,44-48] For example, the PEDOT-PSS (poly(styrenesulfonate)) modified mesoporous carbon/sulfur particles only displays a capacity of 600 mAh g^{-1} after 60 cycles at 0.2 C.[47] Sulfur NPs supported by multi-walled carbon nanotubes and coated with polyaniline as cathode has been demonstrated with a capacity of ~580 mAh g^{-1} after 100 cycles at 0.2 C.[48]

Fig. 5b presents the cycling performance of the S@PEDOT/MnO_2 electrode at high current densities of 0.5 and 1.0 C for 200 cycles, respectively. It demonstrates the specific discharge capacity of 910 mAh g^{-1} at 0.5 C for the first cycle. After 200 cycles, a discharge capacity of 545 mAh g^{-1} with capacity retention of 59.9% is obtained. At a higher current density of 1.0 C, a stable cycling performance is observed with an initial capacity of 685 mAh g^{-1} and a reverse capacity ~360 mAh g^{-1} after 200 cycles, corresponding to 52.5% capacity retention. Those electrochemical performance also have been summarized in the inset bar graph of Fig. 5b. The remarkable capacities and cyclability at high current densities indicate the double shell structure can help to immobilize the polysulfides and mitigate capacity fading. Fig. 5c shows the discharge-charge profiles of S@PEDOT/MnO_2 electrodes at different current densities of 0.5 and 1.0 C. It can be seen that, the discharge profiles at both current densities show two plateaus around 2.0 and 2.3 V, which are maintained even at high current density of of 2.0 C, suggesting little kinetic barrier in the electrode reaction.

The rate capabilities of the S-NPs, S@PEDOT, and S@PEDOT/MnO_2 electrodes are further investigated to examine the effectiveness of MnO_2-NSs modification (Fig. 5d). The discharge capacities gradually decrease as the rate is increased from 0.2 C to 3.0 C for these three electrodes. Again, the S@PEDOT/MnO_2 electrode exhibits superior rate property at different current densities, delivering the discharge capacities of 1164, 1002, 896, 767 and 631 mAh g^{-1} at the current densities of 0.2, 0.5, 1.0, 2.0 and 3.0 C, respectively. When the current density backs to 0.2 C, a reversible capacity of 1005 mAh g^{-1} can still be obtained with a capacity retention of 86.3 %, suggesting its perfect stability and excellent reversibility at different rates. However, the S@PEDOT composite without MnO_2 functionalization shows an inferior performance with the reversible capacities of 1045, 835, 667, 480, and 297 mAh g^{-1} at 0.2, 0.5, 1.0, 2.0 and 3.0 C, respectively. Obviously, the S@PEDOT/MnO_2 composite can effectively diminish the disadvantages of S-NPs and S@PEDOT, indicating that the unique double shell S@PEDOT/MnO_2 composite with metal oxide-polymer modification has improved Li^+ diffusion efficiency and is relatively stable at a high current density. In addition, both the PEDOT electron conducting network and MnO_2 coating layer act as effective physical barrier to restrain the yielded polysulfides, promoting the utilization of the active material and the reaction kinetics, and further the charge transportation (Fig. 1g).

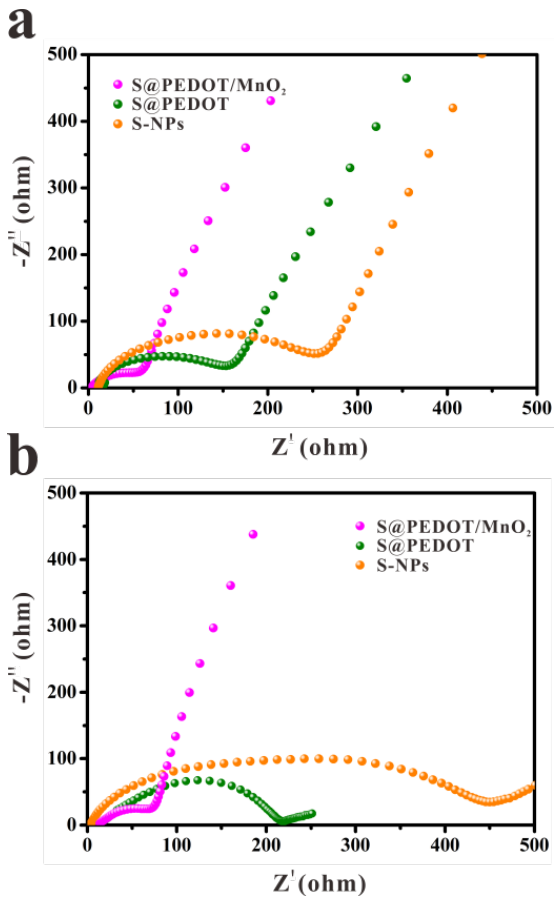

Fig. 6 EIS spectra of S-NPs, S@PEDOT, and S@PEDOT/MnO_2 electrodes before (a) and after (b) 200 cycles.

To further clarify the improving effect of double modification (metal oxide-polymer) of S@PEDOT/MnO_2 composites, the electrochemical impedance spectroscopy (EIS) tests of S-NPs, S@PEDOT, and S@PEDOT/MnO_2 electrodes are conducted before and after 200 cycles. Before cycling, it can be seen that the impedance plots for all of the open-circuit

potential states are composed of a depressed semicircle in the high-frequency domain and a sloping/straight line in the low-frequency region (Fig. 6a). The semicircle in the high-frequency domain corresponds to the charge-transfer process, which reflects the resistance over Li^+ diffusion through the contacting interface. The straight line in the low-frequency domain corresponds to a semi-infinite warburg diffusion process. A lower charge transfer resistance (R_{ct}) means more conducive to electrochemical reaction kinetics. Obviously, S@PEDOT/MnO_2 exhibits a much lower R_{ct} (59 Ω) than those of S@PEDOT (155 Ω) and S-NPs (260 Ω), indicating that the conducting PEDOT and MnO_2-NSs shell facilitates electrical conduction and reduces the R_{ct}. This benefits to improve the electron and ion kinetics in the composite electrode, consequently, enhancing the electrochemical performance of S@PEDOT/MnO_2 electrode. As presented in Fig. 6b, after cycling for 200 times, the total impedance gradually increase with the increase of cycling number. The R_{ct} value of the S@PEDOT/MnO_2 electrode increases to 71 Ω, showing a 20% increase (Table S1, ESI†). The R_{ct} values of the S@PEDOT and S-NPs electrodes increase to 218 and 450 Ω, demonstrating an increasement of 41% and 73%, respectively (Table S1, ESI†). These results verify that S@PEDOT/MnO_2 has more conductive and stable structure than S@PEDOT and S-NPs, leading to the less R_{ct} change than those of S@PEDOT and S-NPs, and exhibits the best electrochemical performance among the three samples.

To clearly show the advantage of the MnO_2 nanosheets modification of S@PEDOT, we have used SEM to observe the S-NPs, S@PEDOT and S@PEDOT/MnO_2 electrodes after 200 cycles at 0.2 C. Fig. 7 shows the SEM images of the three electrodes before and after cycling. For the S-NPs electrode, the sulfur nanoparticles can be obviously seen (Fig. 7a). However, after cycling, there is no single sulfur nanoparticle in the electrode (Fig. 7b). This indicates that the yielded polysulfides are easily dissolved into the organic electrolyte and then diffuse to the anode side during cycling process. The loss of active material leads to poor electrochemical performance. After coating PEDOT on S-NPs, the morphology of S@PEDOT is mainly maintained after 200 cycles at 0.2 C (Fig. 7c and 7d). It is interesting to see that there are some flat areas in the cycled S@PEDOT electrode. Most possibly, these flat areas are the broken S-NPs from the S@PEDOT nanoparticles. This means that the PEDOT coating can partly prevent sulfur loss, still leading to capacity fading during the

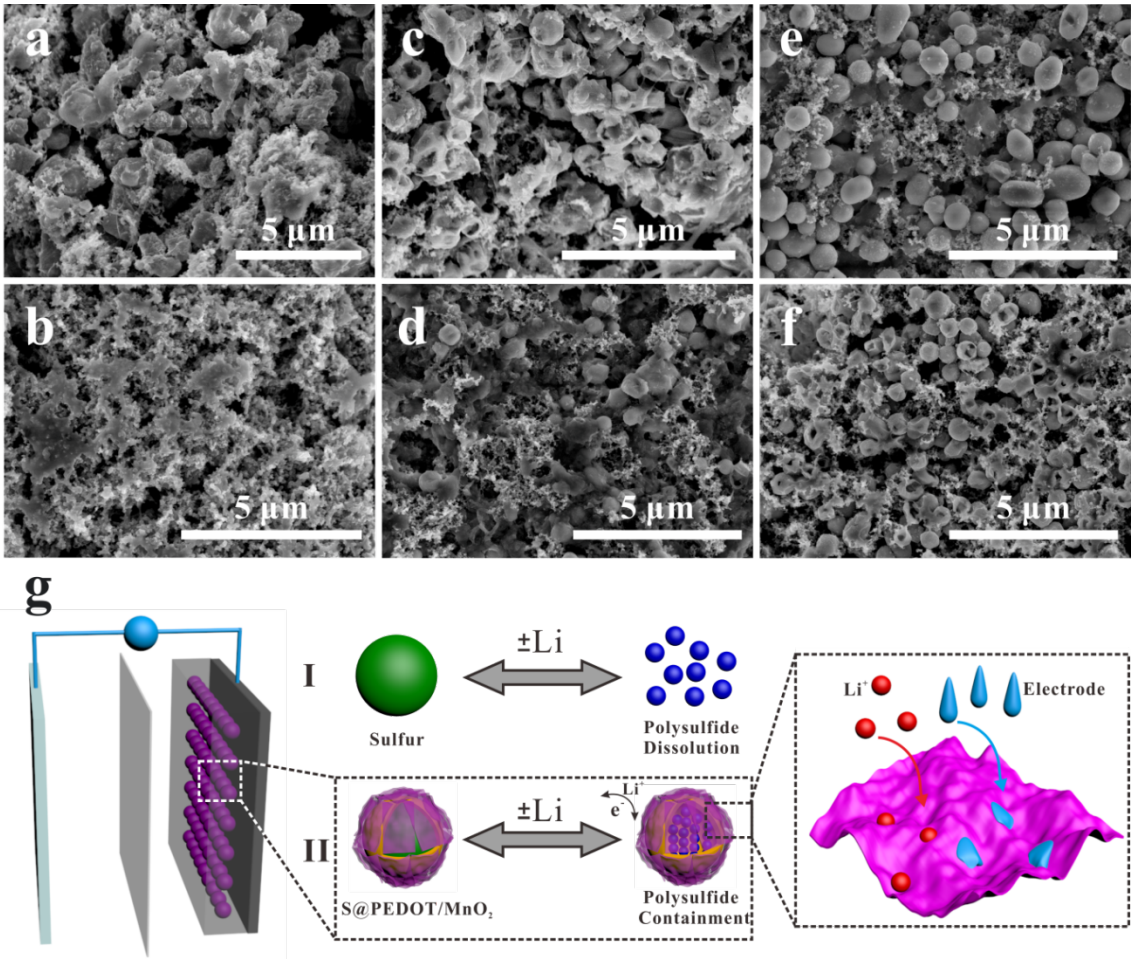

Fig. 7 SEM images of (a, b) S-NPs, (c, d) S@PEDOT and (e, f) S@PEDOT/MnO_2 electrodes before and after running for 200 cycles at 0.2 C in coin cells. (g) A schematic illustration of working mechanism on the S@PEDOT/MnO_2 electrode. Proper pathways for electron transfer in the discharge stage have also been displayed.

cycling process. Fig. 7e and 7f present the S@PEDOT/MnO_2 electrode before and after running 200 cycles in coin cells, respectively. They clearly show that the S@PEDOT/MnO_2 nanoparticles still keep the original morphology. This directly verifies that the MnO_2 functionalization of PEDOT shell effectively prevents electrode degradation. Thus the S@PEDOT/MnO_2 electrode shows highly improved electrochemical performance and structural stability.

To show the different solubility behaviour, we have soaked the three electrodes in ethanol for 5 min to clarify the polysulfides dissolution before and after 200 cycles. The digital photographs of the electrode in ethanol are shown in Fig. S1 (ESI†). It can be seen that the S-NPs, S@PEDOT and S@PEDOT/MnO2 electrodes have transparent solution before cycling (Fig. S1a-c, ESI†). However, the solution colors of the cycled S-NPs (Fig. S1d, ESI†) and S@PEDOT (Fig. S1e, ESI†) quickly turn into yellow and pale-yellow, respectively. This means the easy dissolution of polysulfides without effective encapsulation for S-NPs and S@PEDOT. On the contrary, the solution of the cycled S@PEDOT/MnO_2 is still transparency (Fig. S1c and 1f, ESI†), indicating that double shell of MnO_2 and PEDOT can truly act as barrier to effectively confine the sulfur/polysulfides rather than to dissolve them into the organic electrolyte.

On the basis of above observations and analyses, a S@PEDOT/MnO_2 composite with good rate capability and cycling stability is successfully constructed. The remarkable electrochemical performance should be ascribed to the unique core-shell structure with double metal oxide and polymer modification. We propose a working mechanism of the S@PEDOT/MnO_2 electrode in Li-S batteries, as illustrated in Fig. 7g. For S-NPs electrode, sulfur without encapsulation directly contacts the electrolyte. This produces soluble polysulfides and leads to serious shuttle effect as well as the further lossing of active material. On the contrary, after PEDOT coating, the polysulfides dissolution can be partly prevented. In particular, the S@PEDOT/MnO_2 demonstrates highly enhanced performance, benefitting from the combined advantages of both PEDOT and MnO_2-NSs as following: (1) The PEDOT provides high electrical conductivity and good electrochemical stability; (2) The growth of MnO_2-NSs over PEDOT chains enhances the conductivity and stability of the composite by interlinking the polymer chains and providing high active surface area to improve the wettability electrode material by the electrolyte and to enhance the reaction kinetics; (3) The amorphous MnO_2 nanosheets adsorb cations (Li^+) on the electrode surface from electrolyte and provide a short diffusion path, making the PEDOT layer serve as a fast path for electron transport; (4) The double shell of PEDOT and MnO_2-NSs act as effective protective layers to entrap the active polysulfides inside the cathode.

4. Conclusions

In summary, a MnO_2-NSs functionalized core-shell S@PEDOT/MnO_2 heterostructure with ~87 wt% sulfur content is designed for advanced Li-S batteries. This unique core-shell nanostructure helps to trap the yielded polysulfides and minimize their dissolution. Further, the growth of MnO_2-NSs on PEDOT via interlinking the polymer chains can provide high active surface area to increase the wettability of the active materials with the electrolyte and further enhance the conductivity and stability of the composite. Benefiting from these advantages, the core-shell S@PEDOT/MnO_2 heterostructure demonstrates a highly enhanced electrochemcial performance comparing to other samples. A discharge capacity of 827 mAh g^{-1} after 200 cycles at 0.2 C is maintained. In particular, the discharge capacity of S@PEDOT/MnO_2 is 545 mAh g^{-1} after 200 cycles at 0.5 C. Our demonstration here indicates that inorganic nanostructures functionalizing conducting polymer coated sulfur nanoparticles is an effective strategy to restrain the reaction kinetic hindrance and to improve the electrochemical cycling performance and stability of sulfur cathodes for Li-S batteries. We believe that our simple strategy is an effective technique for improving the electrochemical cycling performance and stability of electrodes in Li-S batteries.

Acknowledgements

B. L. Su acknowledges the Chinese Central Government for an "Expert of the State" position in the Program of the "Thousand Talents" and a Life Membership at the Clare Hall and the financial support of the Department of Chemistry, University of Cambridge. Y. Li and L. H. Chen acknowledges Hubei Provincial Department of Education for the "Chutian Scholar" program. T. Hasan acknowledges support from the Royal Academy of Engineering (Graphlex). This work is supported by Program for Changjiang Scholars and Innovative Research Team in University (IRT_15R52), Hubei Provincial Natural Science Foundation (2014CFB160 and 2015CFB428), the National Natural Science Foundation of China (No. 21301133) and International Science & Technology Cooperation Program of China (2015DFE52870).

Notes and references

1 B. Scrosati, *Nature*, 1995, **373**, 557-558.
2 G. Ceder, Y. M. Chiang, D. R. Sadoway, M. K. Aydinol, Y. I. Jang and B. Huang, *Nature*, 1998, **392**, 694-696.
3 M. Armand and J. M. Tarascon, *Nature*, 2008, **451**, 652-657.
4 P. G. Bruce, S. A. Freunberger, L. J. Hardwick and J. M. Tarascon, *Nat. Mater.*, 2012, **11**, 19-29.
5 Y. Wang, L. Huang, L. Sun, S. Xie, G. Xu, S. Chen, Y. Xu, J. Li, S. Chou, S. Dou and S. Sun, *J. Mater. Chem.*, 2012, **22**, 4744-4750.
6 J. Gao, M. A. Lowe, Y. Kiya and H. D. Abruña, *J. Phys. Chem. C*, 2011, **115**, 25132-25137.
7 X. Ji and L. F. Nazar, *J. Mater. Chem.*, 2010, **20**, 9821-9826.
8 X. Wang, G. Li, J. Li, Y. Zhang, A. Wook, A. Yu and Z. Chen, *Energ. Environ. Sci.*, 2016, DOI: 10.1039/C6EE00194G.
9 X. Liang, C. Hart, Q. Pang, A. Garsuch, T. Weiss and L. F. Nazar, *Nat. Commun.*, 2015, **6**, 5682-5689.
10 S. Lim, R. Lilly Thankamony, T. Yim, H. Chu, Y.-J. Kim, J. Mun, T.-H. Kim, *ACS Appl. Mater. Inter.*, 2015, **7**, 1401-1405.
11 Tang, B. Q. Li, Q. Zhang, L. Zhu, H. F. Wang, J. L. Shi and F. Wei, *Advanced Functional Materials*, 2016, 26, 577-585.

12 Q. Zhao, X. Hu, K. Zhang, N. Zhang, Y. Hu and J. Chen. *Nano Lett.,* 2015, **15**, 721−726.
13 Z. Yuan, H. J. Peng, T. Z. Hou, J. Q. Huang, C. M. Chen, D. W. Wang, X. B. Cheng, F. Wei and Q. Zhang, *Nano lett.*, 2016, **16**, 519-527.
14 Z. Zhang, Q. Li, K. Zhang,Y. Lai and J. Li, *Electrochim. Acta,* 2015, **152**, 53-60.
15 Z. Wei Seh, W. Li, J. J. Cha, G. Zheng, Y. Yang, M. T. McDowell, P. C. Hsu and Y. Cui, *Nat. Commun.*, 2013, **4**, 1331.
16 X. Ji, K. T. Lee and L. F. Nazar, *Nat. Mater.*, 2009, **8**, 500-506.
17 R. Elazari, G. Salitra, A. Garsuch, A. Panchenko and D. Aurbach, *Adv. Mater.*, 2011, **23**, 5641-5644.
18 G. Zhou, D. W. Wang, F. Li, P. X. Hou, L. Yin, C. Liu, G. Q. Lu, I. R. Gentle and H.-M. Cheng, *Energy & Environ. Sci.*, 2012, **5**, 8901-8906.
19 J. Schuster, G. He, B. Mandlmeier, T. Yim, K. T. Lee, T. Bein and L. F. Nazar, *Angew. Chem. Int. Edit.*, 2012, **51**, 3591-3595.
20 C. Zhang, H. B. Wu, C. Yuan, Z. Guo and X. W. Lou, *Angew. Chem. Int. Edit.*, 2012, **51**, 9592-9595.
21 Y. S. Su and A. Manthiram, *Nat. Commun.*, 2012, **3**, 542-555.
22 W. Li, Q. Zhang, G. Zheng, Z. W. Seh, H. Yao and Y. Cui, *Nano Lett.,* 2013, **13**, 5534-5540.
23 J. H. Kim, K. Fu, J. Choi, K. Kil, J. Kim, X. Han, L. Hu and U. Paik, *Sci. Rep.*, 2015, **5**, 8946.
24 C. Wang, H. Chen, W. Dong, J. Ge, W. Lu, X. Wu, L. Guo and L. Chen, *Chem. Commun.*, 2014, **50**, 1202-1204.
25 Y. Sun, S. Wang, H. Cheng, Y. Dai, J. Yu and J. Wu, *Electrochim. Acta*, 2015, **158**, 143-151.
26 2H. Li, M. Sun, T. Zhang, Y. Fang and G. Wang, *J. Mater. Chem. A*, 2014, **2**, 18345-18352.
27 X. Wang, Z. Zhang, X. Yan, Y. Qu, Y. Lai and J. Li, *Electrochim. Acta*, 2015, **155**, 54-60.
28 Y. Deng, H. Xu, Z. Bai, B. Huang, J. Su and G. Chen, *J. Power Sources*, 2015, **300**, 386-394.
29 L. Wang, Z. Dong, D. Wang, F. Zhang and J. Jin, *Nano Lett.*, 2013, **13**, 6244-6250.
30 G. Ma, Z. Wen, J. Jin, M. Wu, X. Wu and J. Zhang, *J. Power Sources*, 2014, **267**, 542-546.
31 Y. Fu and A. Manthiram, *J. Phys. Chem. C*, 2012, **116**, 8910-8915.
32 X. Li, M. Rao, H. Lin, D. Chen, Y. Liu, S. Liu, Y. Liao, L. Xing, M. Xu and W. Li, *J. Mater. Chem. A*, 2015, **3**, 18098-18104.
33 W. Li, G. Zheng, Y. Yang, Z. W. Seh, N. Liu and Y. Cui, *Proc. Natl. Acad. Sci.*, 2013, **110**, 7148-7153.
34 X. Liang, M. Zhang, M. R. Kaiser, X. Gao, K. Konstantinov, R. Tandiono, Z. Wang, H.-K. Liu, S. X. Dou and J. Wang, *Nano Energy*, 2015, **11**, 587-599.
35 F. Wu, J. Chen, R. Chen, S. Wu, L. Li, S. Chen and T. Zhao, *J. Phys. Chem. C*, 2011, **115**, 6057-6063.
36 H. Chen, W. Dong, J. Ge, C. Wang, X. Wu, W. Lu and L. Chen, *Sci. Rep.*, 2013, **3**, 1910.
37 J. Jin, S. Z. Huang, Y. Li, H. Tian, H. E. Wang, Y. Yu, L. H. Chen, T. Hasan and B. L. Su, *Nanoscale*, 2015, **7**, 12979-12989.
38 G. C. Li, G. R. Li, S. H. Ye and X. P. Gao, *Adv. Energy Mater.*, 2012, **2**, 1238-1245.
39 J. Jiang, J. Zhu, W. Ai, X. Wang, Y. Wang, C. Zou, W. Huang and T. Yu, *Nat. Commun.*, 2015, **6**, 8622.
40 A. L. M. Reddy, M. M. Shaijumon, S. R. Gowda and P. M. Ajayan, *Nano Lett.*, 2009, **9**, 1002-1006.
41 B. J. Tan, K. J. Klabunde and P. M. A. Sherwood, *J. Am. Chem. Soc.*, 1991, **113**, 855-861.
42 W. Zhou, Y. Yu, H. Chen, F. J. DiSalvo and H. D. Abruna, *J. Am. Chem. Soc.*, 2013, **135**, 16736-16743.
43 L. Mai, F. Dong, X. Xu, Y. Luo, Q. An, Y. Zhao, J. Pan and J. Yang, *Nano Lett.,* 2013, **13**, 740-745.
44 Y. Zhang, Y. Zhao, Z. Bakenov, M. Tuiyebayeva, A. Konarov and P. Chen, *Electrochimic. Acta,* 2014, **143**, 49-55.
45 X. Zhou, F. Chen and J. Yang, *J. Nat. Gas. Chem.,* 2015, **24**, 448-455.
46 N. Nakamura, T. Yokoshima, H. Nara, T. Momma and T. Osaka, *J. Power Sources*, 2015, **274**, 1263-1266.
47 Y. Yang, J. J. Cha, S. S. Hong and Y. Cui, *Nano Lett.*, 2011, **11**, 4462-4467.
48 X. Li, M. Rao, D. Chen, H. Lin, Y. Liu, Y. Liao, L. Xing and W. Li, *Electrochim. Acta*, 2015, **166**, 93-99.

Supporting Information

Manganese Dioxide Nanosheets Functionalizing Sulfur@PEDOT Core-Shell Nanospheres for Advanced Lithium-Sulfur Batteries

Min Yan,[a] Yang Zhang,[a] Yu Li,[a]* Yongqi Huo,[a] Yong Yu,[a] Chao Wang,[a] Jun Jin,[a] Lihua Chen,[a] Tawfique Hasan,[b] Binjie Wang[c] and Bao-Lian Su[a,d,e]*

[a] *State Key Laboratory of Advanced Technology for Materials Synthesis and Processing, Wuhan University of Technology, 122 Luoshi Road, 430070, Wuhan, Hubei, China; Fax:+86 27 87879468; Tel: +86 27 87855322; Email: yu.li@whut.edu.cn and baoliansu@whut.edu.cn*

[b] *Cambridge Graphene Centre, University of Cambridge, 9 JJ Thomson Avenue, Cambridge CB3 0FA, United Kingdom*

[c] *FEI Company, Shanghai Nanoport, 399 Shengxia Road, 201210 Shanghai, China*

[d] *Laboratory of Inorganic Materials Chemistry (CMI), University of Namur, 61 rue de Bruxelles, B-5000 Namur, Belgium; Fax: +32 81 725414; Tel: +32 81 724531; E-mail: bao-lian.su@unamur.be*

[e] *Department of Chemistry and Clare Hall, University of Cambridge, Cambridge, CB2 1EW, United Kingdom; E-mail: bls26@cam.ac.uk*

Table S1 R_{ct} values and increasements of the S-NPs, S@PEDOT and S@PEDOT/MnO_2 electrodes before and after 200 cycles

R_{ct}	S (Ω)	S@PEDOT (Ω)	S@PEDOT/MnO_2 (Ω)
0 cycle	260	155	59
The 200th cycle	450	218	71
Increasement (%)	73	41	20

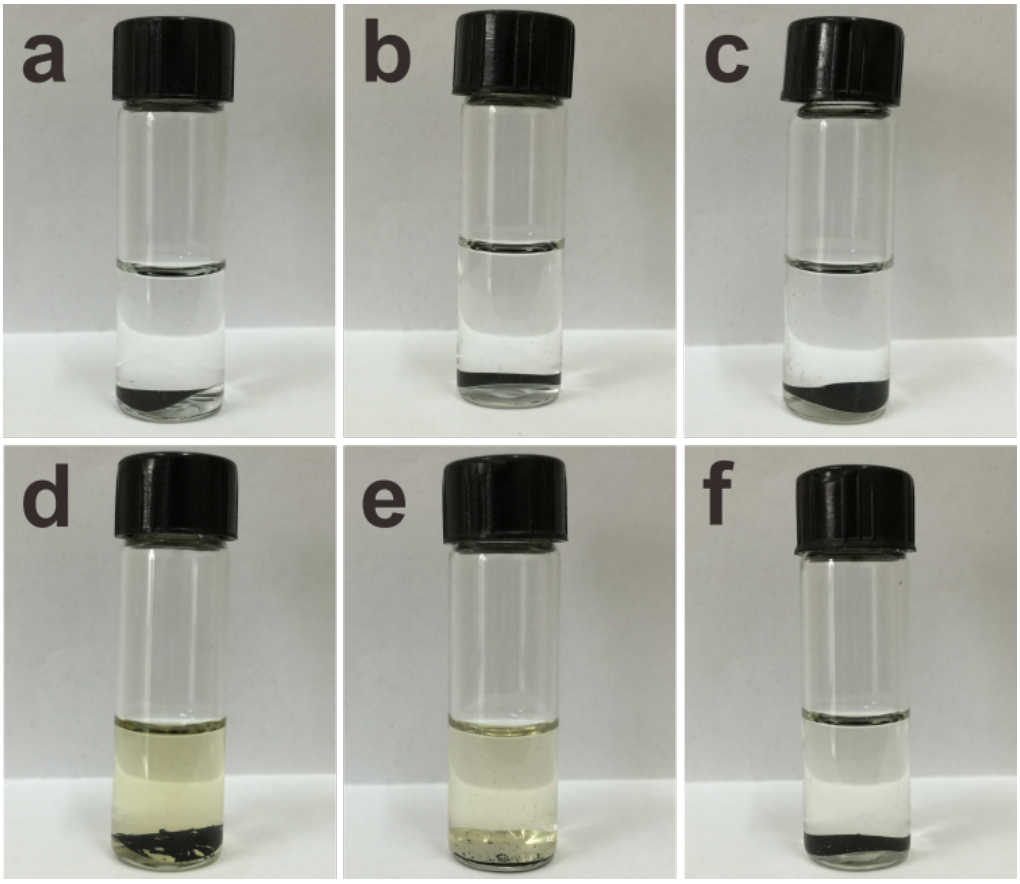

Fig. S1 Digital photographs of (a, d) S-NPs, (b, e) S@PEDOT, and (c, f) S@PEDOT/MnO_2 electrodes in ethanol before and after 200 cycles.